

## RESEARCH ARTICLE

10.1002/2017JB015169

## Key Points:

- Single-crystal X-ray diffraction experiments are carried out on hydrous Mg end-member and Ni-bearing orthoenstatite(oEn) to 30 GPa and 700 K
- Several hundred ppm of water has negligible effects on the phase transition and bulk modulus of oEn but promotes the thermal expansion
- Ni<sup>2+</sup> strongly influences the phase transition of oEn and causes a different high-pressure transition ( $\beta$ -opx $\rightarrow$  $\beta$ -opxII) than that in Fe-oEn

## Supporting Information:

- Supporting Information S1
- Table S1
- Table S2
- Table S3
- Table S4

## Correspondence to:

D. Fan and P. Dera,  
 fandawei@vip.gyig.ac.cn;  
 pdera@hawaii.edu

## Citation:

Xu, J., Zhang, D., Fan, D., Zhang, J. S., Hu, Y., Guo, X., et al. (2018). Phase transitions in orthoenstatite and subduction zone dynamics: Effects of water and transition metal ions. *Journal of Geophysical Research: Solid Earth*, 123, 2723–2737. <https://doi.org/10.1002/2017JB015169>





Received 29 OCT 2017

Accepted 16 MAR 2018

Accepted article online 23 MAR 2018

Published online 13 APR 2018

## Phase Transitions in Orthoenstatite and Subduction Zone Dynamics: Effects of Water and Transition Metal Ions

Jingui Xu<sup>1,2,3</sup>, Dongzhou Zhang<sup>2</sup> , Dawei Fan<sup>1</sup>, Jin S. Zhang<sup>4</sup> , Yi Hu<sup>2</sup> , Xinzhan Guo<sup>5</sup>, Przemyslaw Dera<sup>2</sup> , and Wenge Zhou<sup>1</sup>

<sup>1</sup>Key Laboratory of High Temperature and High Pressure Study of the Earth's Interior, Institute of Geochemistry, Chinese Academy of Sciences, Guiyang, China, <sup>2</sup>Hawaii Institute of Geophysics and Planetology, School of Ocean and Earth Science and Technology, University of Hawaii at Manoa, Honolulu, HI, USA, <sup>3</sup>University of Chinese Academy of Sciences, Beijing, China, <sup>4</sup>Institute of Meteoritics, Department of Earth and Planetary Sciences, University of New Mexico, Albuquerque, NM, USA, <sup>5</sup>State Key Laboratory of Geological Processes and Mineral Resources, China University of Geoscience, Wuhan, China

**Abstract** Synchrotron-based high-pressure and temperature single-crystal X-ray diffraction experiments were conducted on two hydrous orthoenstatite samples (oEn#1: Mg<sub>1.004</sub>Si<sub>0.996</sub>O<sub>3</sub>, ~619 ppm water; oEn#2: Mg<sub>0.947</sub>Ni<sub>0.055</sub>Si<sub>0.998</sub>O<sub>3</sub>, ~696 ppm water) to ~34 GPa and 700 K, using resistively heated diamond anvil cells. The  $\alpha$ -opx (*Pbca* space group) $\rightarrow$  $\beta$ -opx (*P2<sub>1</sub>/c* space group) phase transition of oEn#1 occurs at 12.90(2) GPa, and the  $\beta$ -opx phase persists to 34.25(1) GPa. The  $\alpha$ - $\beta$  transition of oEn#2 occurs at 13.50(1) GPa, and a new isosymmetric  $\beta$ -opx $\rightarrow$  $\beta$ -opxII transition takes place at 29.80(4) GPa. The  $\beta$ -opxII phase is preserved down to 24.53(3) GPa during decompression. The transition to the monoclinic  $\beta$ -opxII phase is interpreted as a result of incorporation of Ni<sup>2+</sup> into the orthoenstatite structure. Fitting the third-order Birch-Murnaghan thermal equation of state to the single-crystal P-V-T data yields the thermoelastic parameters of the  $\alpha$ - and  $\beta$ -opx phases for both orthoenstatite samples. This study is the first attempt to determine the thermal equation of state of the  $\beta$ -opx phase. Our results suggest that several hundred ppm of water has negligible effects on the bulk modulus of orthoenstatite but notably enhances the thermal expansion. The potential effects of metastable orthoenstatite on subduction zone dynamics are discussed, and the possible contributions of displacive phase transitions to enhancement of the transformational faulting mechanism of the deep-focus earthquakes in subducted slabs are considered. The presence of metastable orthoenstatite within cold slabs could promote slab stagnation above the 660-km discontinuity.

## 1. Introduction

MgSiO<sub>3</sub> is one of the most abundant chemical compounds present in the mantle of the Earth and other rocky planets (Anderson, 1989). Major structure types characteristic of deep planetary interior and able to accommodate this composition include pyroxene (enstatite), ilmenite (akimotoite), perovskite (bridgmanite), and postperovskite (e.g., Fei & Bertka, 1999; Walter et al., 2011). Orthoenstatite (oEn, space group *Pbca*) is a low-pressure orthopyroxene (opx) polymorph of MgSiO<sub>3</sub>. Opx family with compositions of (Mg<sub>1-x</sub>Fe<sub>x</sub>)SiO<sub>3</sub> is an important component of Earth's upper mantle (Frost, 2008; Ringwood, 1982). Opx is also a major constituent of harzburgite and lherzolite, which are important petrological components of subducting slabs (Frost, 2008; Ringwood, 1982). At high pressure and temperature (7.28(9) GPa and >1000 K), oEn<sub>100</sub> transforms to monoclinic (space group *C2/c*) clinoenstatite (cEn) (e.g., Akashi et al., 2009; Shinmei et al., 1999; Woodland, 1998). oEn<sub>100</sub> transforms to protoenstatite (pEn) (space group *Pbcn*) at ambient pressure and high temperatures (~1400 K) (Murakami et al., 1982; Smyth, 1971), and a different high-temperature phase (*Cmca* space group) has been reported at ~1363 K (Jackson et al., 2004).

At room temperature, pressure-induced phase transitions of opx are complex and several metastable polymorphs have been reported (Finkelstein et al., 2015; Jahn, 2008; Lin, 2004; Lin et al., 2005; Zhang, Jackson, et al., 2013; Zhang et al., 2011; Zhang & Bass, 2016; Zhang et al., 2012). oEn<sub>87</sub> opx transforms to a monoclinic phase (*P2<sub>1</sub>/c*) named  $\beta$ -opx (the ambient opx phase was named as  $\alpha$ -opx, Dera, Finkelstein, et al. (2013) at pressures between 10 and 14 GPa, and the transition pressure depends on the composition (Zhang, Reynard, et al., 2013). At higher pressures two further polymorphs (named  $\alpha$ -post-opx [ $\alpha$ -popx] and  $\beta$ -post-opx [ $\beta$ -popx]) of oEn<sub>90</sub> with space group *Pca2<sub>1</sub>* were reported at 29.9 and 40.3 GPa (Finkelstein et al., 2015). According to this phase-naming convention, opx refers to phases in which the original tetrahedral coordination of Si<sup>4+</sup> is preserved, whereas in popx (post-opx) phases the coordination number of Si

increases to a mixture of IV and V or VI. The  $\beta$ -opx phase has monoclinic symmetry, but the opx (instead of cpx) designation emphasizes preservation of the orthopyroxene stacking.

Fe-rich opx ( $\text{En}_{16}$ ) transforms to the  $\beta$ -opx phase at 11.1(1) GPa, and the second transition occurs at 13.0(1) GPa, to a phase with *Pbca* symmetry named  $\gamma$ -opx (Dera, Finkelstein, et al., 2013). Fe-end-member opx, ferrosilite ( $\text{FeSiO}_3$ ,  $\text{oFs}_{100}$ ), was found to undergo a reconstructive transition at  $\sim 4.2$  GPa and room temperature, and the high-pressure phase has a space group of *C2/c* (Hugh-Jones et al., 1996).

For the Mg end-member opx, previous high-pressure powder X-ray diffraction and Raman spectroscopy studies observed two phase transitions at pressures of about 7–15 GPa and 38–40 GPa, respectively (Lin et al., 2005; Serghiou et al., 2000). Molecular dynamics simulations predicted two high-pressure phase transitions from the original *Pbca* structure to metastable *P2<sub>1</sub>ca* and *Pbca* at  $\sim 9$  GPa and  $\sim 20$  GPa, respectively (Jahn, 2008).

Based on this evidence it is clear that the transition metal cations like  $\text{Fe}^{2+}$  can strongly influence the phase transition pressure and the structure of the high-pressure phases in the Ca-poor pyroxene system.  $\text{Ni}^{2+}$  is another transition metal cation that commonly occurs in natural opx, but its content is generally much lower than that of Fe (e.g., Ishimaru & Arai, 2008; Pearson et al., 2003). No reports on the high-pressure phase transitions in Ni-bearing opx are available.

Studies of natural and synthetic mantle-derived nominally anhydrous minerals (NAMs) suggest that hydrogen could be incorporated in these minerals' crystal structures (e.g., Aubaud et al., 2004; Hirschmann et al., 2005; Warren & Hauri, 2014) and has significant effects on the physical and chemical properties of NAMs (e.g., Chang et al., 2017; Jacobsen, 2006). Among these NAMs, olivine, wadsleyite, and ringwoodite received probably the most attention. Previous studies indicated that water can decrease the pressure of olivine-wadsleyite transition, hence shift the upper mantle-transition zone boundary (Frost & Dolejš, 2007), and increase the pressure of ringwoodite  $\rightarrow$  bridgmanite + ferropericlase transformation (Ghosh et al., 2013; Litasov et al., 2005). The effects of water on the elastic properties of olivine have also been investigated, and 0.8 wt %  $\text{H}_2\text{O}$  reduces the bulk modulus by 6% (Smyth et al., 2005).

Pyroxene is the second most abundant mineral in the upper mantle. Numerous studies have suggested that water contents in pyroxene can be higher than in olivine (e.g., Aubaud et al., 2004; Peslier & Bizimis, 2015; Warren & Hauri, 2014), yet investigations of the effects of water on the phase transitions and elastic properties of pyroxenes are limited. In situ high-pressure single-crystal X-ray diffraction experiments to  $\sim 8$  GPa on synthetic hydrous cEn ( $\text{MgSiO}_3$ ) indicated that  $\sim 900$  ppm water could lower the pressure of the *P2<sub>1</sub>/c-C2/c* phase transition, but the effects on elastic properties are negligible (Jacobsen et al., 2010). Similar investigations of synthetic hydrous diopside ( $\text{CaMgSi}_2\text{O}_6$ ) also showed that  $\sim 600$  ppm water has undetectable effects on elastic properties (Gavrilenko et al., 2010).

Although the phase relations of oEn have been extensively studied at high pressures and temperatures (typically  $>1000$  K) (e.g., Akins et al., 2004; Fei & Bertka, 1999; Hirose et al., 2006; Ito & Navrotsky, 1985; Murakami et al., 2004; Oganov & Ono, 2004; Presnall, 1995), the work on metastable phase evolution of oEn on compression in lower temperature regime ( $<1000$  K) is limited. Understanding the phase transitions at such conditions is of similar/equal importance for modeling the dynamics of the Earth's interior as knowledge about the equilibrium phase relations, because such cold high-pressure conditions are present in old and rapidly subducting slabs. Some geophysical models suggested that relatively low temperatures (below 1000 K) could be retained to a depths as great as  $\sim 800$  km (Bina et al., 2001; Bina & Navrotsky, 2000). In addition, a recent study demonstrated that the thermal conductivity of hydrated olivine would be significantly suppressed at pressures above 5 GPa, suggesting a much colder slab center extending to transition zone depths than previously expected (Chang et al., 2017). Such cold slab center temperatures could allow metastable olivine and pyroxene to survive thermally insulated to depths greater than considered before (Mosenfelder et al., 2001; Nishi et al., 2013; Van Mierlo et al., 2013). Several experiments have demonstrated that dissolution of pyroxene in garnet is much slower than the olivine phase transitions (e.g., Nishi et al., 2008, 2013; Van Mierlo et al., 2013); the metastable persistence of pyroxene in subducted slabs is therefore more likely than that of any other low-pressure mineral phases. Recent studies have suggested that the presence of metastable pyroxenes could cause some slabs to stagnate above the 660 km discontinuity (Agrusta et al., 2014; Bina, 2013; King et al., 2015;

Nishi et al., 2013; Van Mierlo et al., 2013; Xu, Zhang, Dera, et al., 2017; Xu, Zhang, Fan, et al., 2017). Therefore, studying opx at high pressures and temperatures relevant to cold slab conditions is imperative to understanding the subduction zone dynamics.

In this study, we used single-crystal X-ray diffraction method combined with resistively heated diamond anvil cells (DACs) to study the phase evolutions of hydrous oEn and Ni-oEn at high pressures and temperatures, simulating conditions within the coldest part of a subducting slab.

## 2. Materials and Methods

### 2.1. Synthesis of Hydrous oEn

Two H<sub>2</sub>O-bearing oEn samples (oEn#1 and oEn#2) were synthesized in a multi-anvil pressure apparatus at the Institute of Geochemistry, Chinese Academy of Sciences, Guiyang, China. The sample assembly was similar to that described by Zhou et al. (2001). A stoichiometric mixture of high purity MgO and SiO<sub>2</sub> was used for the starting material and was encapsulated in a platinum capsule with 13 wt % ultrapure water. In order to obtain Ni-bearing oEn samples, a Ni foil was used as the oxygen buffer in the synthesis of the oEn#2 samples, as described by Rauch and Keppler (2002), while no oxygen fugacity buffer was used in synthesis of oEn#1. High pressure was generated by simultaneously advancing six hydraulic rams as described by Fan et al. (2013). Pressure was calibrated using melting curves of Au (Fu & Zhu, 1980) and four other metals (Cu, Al, Pb, and Zn) (Shan et al., 2007), and the pressure measurement error margin is less than 1.5%. High temperatures were generated by a graphite heater and measured by a W<sub>95</sub>Re<sub>5</sub>-W<sub>74</sub>Re<sub>26</sub> thermocouple, and the temperatures during the experiment fluctuated within ±5 K. During synthesis of oEn#2, the sample was first compressed to 3.5 GPa over 35 min and then heated to 1623 K with a heating time of 30 min. After run duration of 75 h at 3.5 GPa and 1623 K, the oEn crystals (100–400 μm size) were obtained from the quenched run product. During synthesis of oEn#1, the starting material was first compressed to 3.2 GPa and then heated to 1393 K at the same compression and heating rates as for oEn#2, the run duration time was 2 hr, and the obtained crystals (50–150 μm size) were smaller than oEn#2.

### 2.2. Electron Microprobe and FTIR Analysis

Selected crystals (about 100 and 300 μm for oEn#1 and oEn#2, respectively) were used for chemical analysis by electron microprobe. A JEOL Hyperprobe JXA-8500F microscope was used for analysis, operating at a 15 kV accelerating voltage and 20 nA beam current, and the beam size of 10 μm. The results suggested chemical formulas of [Mg<sub>1.004</sub>Si<sub>0.996</sub>O<sub>3</sub>] and [Mg<sub>0.947</sub>Ni<sub>0.055</sub>Si<sub>0.998</sub>O<sub>3</sub>] for oEn#1 and oEn#2, respectively.

Analysis of water in oEn was conducted by unpolarized Fourier transform infrared (FTIR) measurements. Normally, quantitative FTIR measurements of water content for anisotropic crystals require measurements of polarized spectra along the crystallographic axes *a*, *b*, and *c* (e.g., Bell et al., 1995; Rauch & Keppler, 2002). However, unpolarized measurements were also used in a few cases, depending on the samples, especially for quenched crystals from high-pressure synthesis (e.g., Jacobsen et al., 2010; Padrón-Navarta et al., 2014; Rauch & Keppler, 2002). Infrared spectra were acquired using a Bruker Vertex FTIR spectrometer coupled with a Hyperion 2000 microscope. FTIR measurements on double polished crystals (~40 μm in thickness for oEn#1; ~85 μm in thickness for oEn#2) were conducted only on optically clean areas and without any inclusions and fractures. The aperture size was 50 × 50 μm. Figures S1a and S1b in the supporting information show the representative infrared spectra of oEn#1 and oEn#2 with random orientation. The sharp absorption features of oEn#2 spectra are very consistent with the hydrous oEn<sub>100</sub> synthesized by Rauch and Keppler (2002), while the spectrum of oEn#1 is different, with relatively broad features, which might indicate complex speciation of water in this sample. The synthetic run duration time of oEn#1 was much shorter than that of oEn#2 and oEn<sub>100</sub> samples from Rauch and Keppler (2002) (40–264 hr), which may be the reason for the observed broad bands of oEn#1. Water content was estimated from the infrared spectra (Figures S1a and S1b), using the mineral-specific calibration factor for opx proposed by Bell et al. (1995) and an orientation factor of  $\frac{1}{3}$  (Paterson, 1982), resulting in ~619 and ~696 weight ppm H<sub>2</sub>O for oEn#1 and oEn#2, respectively. It should be noted that sufficient grains (the more the better) of random orientation are needed for estimations of water contents from unpolarized FTIR measurements of anisotropic crystals (e.g., Rauch & Keppler, 2002). In this study, the number of available crystals with big enough size and free of inclusions was very

limited (one and two for oEn#1 and oEn#2, respectively); therefore, the water contents estimated in this study were more qualitative than quantitative.

### 2.3. Single-Crystal X-Ray Diffraction Experiments and Data Processing

Small chips ( $30 \times 25 \mu\text{m}^2$  for oEn#1 and  $60 \times 40 \mu\text{m}^2$  for oEn#2) of single-crystal samples with thicknesses about  $10 \mu\text{m}$  were extracted from FTIR samples for this study. Single-crystal samples were first mounted onto a polymer micromesh sample holder (MiTeGen) for ambient X-ray diffraction. One single crystal was used for each high-pressure/temperature experiment. In the ambient temperature and high-pressure experiments, a BX90 DAC (Kantor et al., 2012) was used for oEn#1 while a four-pin DAC was used for oEn#2. The BX90 and four-pin DACs were equipped with two Type-I diamonds ( $300 \mu\text{m}$  culets) mounted on Bohler-Almax-type WC seats, and these two DACs had  $\pm 30^\circ$  and  $\pm 34^\circ$  opening angles, respectively. Rhenium gaskets were used and preindented to  $\sim 45 \mu\text{m}$  thicknesses before laser drilling of  $\sim 190 \mu\text{m}$  diameter holes. The single-crystals of oEn#1 and oEn#2 were loaded into the sample chambers with Au as the pressure calibrant (Fei et al., 2007). At each pressure, Au diffraction patterns were collected before and after the sample data collection and the average pressure values were used. A small ruby sphere of  $\sim 10 \mu\text{m}$  was also loaded into each DAC sample chamber and used as the pressure indicator for the gas loading with neon as the pressure-transmitting medium using the GSECARS (GeoSoilEnviroCARS) gas-loading system (Rivers et al., 2008). Externally heated DACs equipped with two  $500 \mu\text{m}$  culet diamonds were used for diffraction experiments at high pressures and temperatures and had  $\pm 17^\circ$  opening angles. High temperatures (up to 600 and 700 K for oEn#1 and oEn#2, respectively) were generated by a resistive-heating system and measured by a K-type thermocouple attached to one of the diamond anvils  $\sim 500 \mu\text{m}$  away from the diamond culet. The gaskets and pressure transmitting media, and pressure calibrants were the same as in the ambient-temperature DACs.

All of the X-ray diffraction experiments were conducted at the experimental station 13-BM-C of the Advanced Photon Source, Argonne National Laboratory. The incident X-ray beam was monochromated to a wavelength of  $0.4340 \text{ \AA}$  and had a focal spot size of  $15 \times 15 \mu\text{m}^2$ . Diffraction images were acquired on a MAR165 CCD (Charge-coupled Device) detector, and the tilting and rotation of the detector and the sample-to-detector distance were calibrated using ambient  $\text{LaB}_6$  powder (Zhang et al., 2017). Multiple detector positions (D1, D2, D3, and D4) were used to obtain adequate number of diffraction peaks. At D1 position the detector is perpendicular to the incident X-ray direction, D2 was achieved by rotating the detector about the horizontal axis by  $20^\circ$ , and D3 and D4 involved rotation of the detector about the vertical axis by  $10^\circ$  and  $-10^\circ$ , respectively. For ambient diffraction experiments, wide and step  $\varphi$ -rotation exposures were collected over a range from  $-90^\circ$  to  $90^\circ$ , and the exposure time was 1 s/deg. Additionally, wide segment exposures with  $10^\circ$  rotation step were collected at each detector position, and the exposure time was 2 s/deg. At high pressure, wide and step  $\varphi$ -rotation exposures were collected in a rotation range depending on the DAC opening angle, and the exposure time was 3 s/deg. Likewise, the wide segment exposures with  $10^\circ$  rotation step were collected at each detector position, while the exposure time was 6 s/deg. The  $\varphi$  scan rotation axis was horizontal and perpendicular to the incident X-ray direction.

Diffraction images were analyzed using the ATREX software package, successor of GSE\_ADA (Dera, Zhuravlev, et al., 2013). The lattice parameters and the orientation matrix were determined with the RSV software, and the reduced reflection data from the four detector positions were merged together. Table S1 shows the unit-cell parameters at each pressure-temperature condition. Crystal structures were refined from the intensity data using the SHELXL software, facilitated by WinGX and Olex 2 user interfaces (Dolomanov et al., 2009; Farrugia, 2012; Sheldrick, 2007). According to the electron microprobe data and previously reported oEn structural model (Periotto et al., 2012), the site occupancies were refined without vacancies. Pyroxenes have a general formula of  $M_2M_1T_2O_6$ , in the structural refinement of oEn#1; the M2, M1, and T sites were set with full occupancy by  $\text{Mg}^{2+}$ ,  $\text{Mg}^{2+}$ , and  $\text{Si}^{4+}$  atoms; and the site occupancies were not refined. In the oEn#2 refinement, M2 and M1 sites were set to fully occupied by a mixture of  $\text{Mg}^{2+}$  and  $\text{Ni}^{2+}$  with refinable ratio. Cations residing at the same site were constrained to share the same atomic displacement parameters and the same fractional coordinates. Because of the limited opening angle ( $\pm 17^\circ$ ) of the externally heated DACs, the structural refinements were not possible, and only unit cell data were used for thermal EoS fitting.

**Table 1**  
Metastable Phase Transformations of Orthopyroxenes

Mineral descriptions	Phase transitions	Pressure range	References
<sup>a</sup> oFs <sub>100</sub> , <i>Pbca</i>	~4.2 GPa, <i>C2/c</i>	0–4.2 GPa	(1)
<sup>b</sup> oEn <sub>87</sub> , <i>Pbca</i>	$\beta$ -opx, 14.26 GPa, <i>P2<sub>1</sub>/c</i>	0–14.53 GPa	(2)
<sup>c</sup> oEn <sub>16</sub> , <i>Pbca</i>	$\beta$ -opx, 11.1(1) GPa, <i>P2<sub>1</sub>/c</i>	$\gamma$ -opx, 13.0(1) GPa, <i>Pbca</i>	(3)
<sup>d</sup> oEn <sub>90</sub> , <i>Pbca</i>	$\beta$ -opx, 14.6 GPa, <i>P2<sub>1</sub>/c</i>	$\alpha$ -popx, 29.9 GPa, <i>Pca2<sub>1</sub></i>	(4)
<sup>e</sup> oEn <sub>100</sub> , <i>Pbca</i>	$\beta$ -opx, 12.90(1) GPa, <i>P2<sub>1</sub>/c</i>	0–34.25 GPa	(5)
<sup>f</sup> oEn <sub>94</sub> , <i>Pbca</i>	$\beta$ -opx, 13.50(1) GPa, <i>P2<sub>1</sub>/c</i>	$\beta$ -opxII, 29.80(4) GPa, <i>P2<sub>1</sub>/c</i>	(6)

Note. References: (1) Hugh-Jones et al. (1996), (2) Zhang et al. (2012), (3) Dera, Finkelstein, et al. (2013), (4) Finkelstein et al. (2015), (5) This study (oEn#1), and (6) This study (oEn#2).

<sup>a</sup>FeSiO<sub>3</sub>. <sup>b</sup>(Mg<sub>0.870</sub>Fe<sub>0.080</sub>Al<sub>0.025</sub>Ca<sub>0.020</sub>Cr<sub>0.005</sub>)(Si<sub>0.970</sub>Al<sub>0.030</sub>)O<sub>3</sub>. <sup>c</sup>(Fe<sub>0.91</sub><sup>2+</sup>Mg<sub>0.93</sub>Ca<sub>0.01</sub>Mn<sub>0.02</sub>Al<sub>0.08</sub>Fe<sub>0.07</sub><sup>3+</sup>)(Si<sub>0.85</sub>Al<sub>0.15</sub>)O<sub>3</sub>. <sup>d</sup>Mg<sub>0.900</sub>Fe<sub>0.088</sub>Ca<sub>0.003</sub>Mn<sub>0.003</sub>Al<sub>0.004</sub>Si<sub>0.999</sub>O<sub>3</sub>. <sup>e</sup>Mg<sub>1.004</sub>Si<sub>0.996</sub>O<sub>3</sub>. <sup>f</sup>Mg<sub>0.947</sub>Ni<sub>0.055</sub>Si<sub>0.998</sub>O<sub>3</sub>.

### 3. Results and Discussion

#### 3.1. Phase Transitions

Diffraction data of oEn#1 and oEn#2 collected at ambient conditions were successfully indexed using the orthorhombic *Pbca*  $\alpha$ -opx unit cell. The unit-cell volume of oEn#2 is slightly smaller than that of oEn#1 (Tables 1 and 2). The ionic radii of Ni<sup>2+</sup> and Mg<sup>2+</sup> are 0.69 and 0.72 Å, respectively (Shannon, 1976), so the difference in the unit cell volume is likely due to the presence of Ni<sup>2+</sup>. The results of the site occupancy refinement for M2 and M1 sites in oEn#2 are consistent with the microprobe analysis (Table S2).

##### 3.1.1. Phase Transitions of Ni-Free oEn#1

Ambient-temperature diffraction data for oEn#1 collected at pressures 0–11.20 GPa were successfully indexed using the unit cell of  $\alpha$ -opx. The diffraction pattern changed with new diffraction peaks appearing at 12.90(2) GPa (Figure S2a). The peaks were indexed with a monoclinic unit cell that has lattice parameters shown in Table S1 and is very similar to  $\beta$ -opx Fe-bearing oEn<sub>87</sub> described by Zhang et al. (2012). This structure change was accompanied by a volume drop of 2.4%. The diffraction data remained consistent with  $\beta$ -opx on compression to 34.25(1) GPa (Table S1). The previously detected pseudomerohedral twinning caused by the  $\alpha$ - $\beta$  opx phase transition in oEn<sub>90</sub> and oEn<sub>16</sub> (Dera, Finkelstein, et al., 2013; Finkelstein et al., 2015) was also observed for oEn#1. The diffraction data collected at 27.40(2) GPa were used to refine the structure of the high-pressure phase of oEn#1, using the model of the  $\beta$ -opx oEn<sub>87</sub>, and the refinement results were satisfactory ( $R_1 = 0.0493$ , see Table S3). Like the  $\beta$ -opx phase of oEn<sub>90</sub>, oEn<sub>87</sub>, and oEn<sub>16</sub>, the  $\beta$  phase of oEn#1 also has a monoclinic *P2<sub>1</sub>/c* symmetry and is structurally closely related to the original  $\alpha$ -opx, as described by Zhang et al. (2012) and Dera, Finkelstein, et al. (2013).

##### 3.1.2. Phase Transitions of Ni-Bearing oEn#2

At room temperature two phase transitions were observed in oEn#2 within the pressure range of 0–29.80 GPa, as indicated by the diffraction patterns (Figure S2B). The first transition occurred between

**Table 2**  
Equation of State Parameters of the  $\alpha$ -opx Phases of Synthetic MgSiO<sub>3</sub> oEn and the  $\beta$  Phases of oEn#1 and oEn#2

Mineral descriptions	$V_0$ (Å <sup>3</sup> )	$K_0$ (GPa)	$K'_0$	$(\partial K_0/\partial T)_P$ (GPa/K)	$\alpha_0 \times 10^{-5}$ (K <sup>-1</sup> )	References
MgSiO <sub>3</sub>	831.4(2)	108(2)	7.9(8)			(1)
MgSiO <sub>3</sub>	832.5(2)	105.8(5)	8.5(3)			(2)
MgSiO <sub>3</sub>	832.7(1)	102.8(2)	10(1)	−0.037(5)	2.9(3)	(3)
MgSiO <sub>3</sub>	832.44(5)	105(3)	7.9(9)	−0.04(2)	5.7(10)	(4)
	832.44(5)	105(3)	8.2(9)			(4) <sup>b</sup>
	810(4)	155(15)	3.1(6)	−0.02(2)	4.7(15)	(4) <sup>a</sup>
	810(5)	154(16)	3.1(7)			(4) <sup>a,b</sup>
Mg <sub>0.947</sub> Ni <sub>0.055</sub> Si <sub>0.998</sub> O <sub>3</sub>	832.02(7)	110(1)	7.0(4)	−0.044(7)	5.3(4)	(5)
	832.02(7)	110(2)	7.1(6)			(5) <sup>b</sup>
	807(6)	165(24)	3(1)	−0.03(1)	3.5(8)	(5) <sup>a</sup>
	806(7)	170(31)	3(2)			(5) <sup>a,b</sup>
	806(7)	170(31)	3(2)			(5) <sup>a,b</sup>

Note. References: (1) Periotto et al. (2012), (2) Angel and Jackson (2002), (3) Zhao et al. (1995), and (4) and (5) are oEn#1 and oEn#2 in this study.

<sup>a</sup> $\beta$  phases derived from ambient temperature data. <sup>b</sup>Results derived from ambient temperature data.

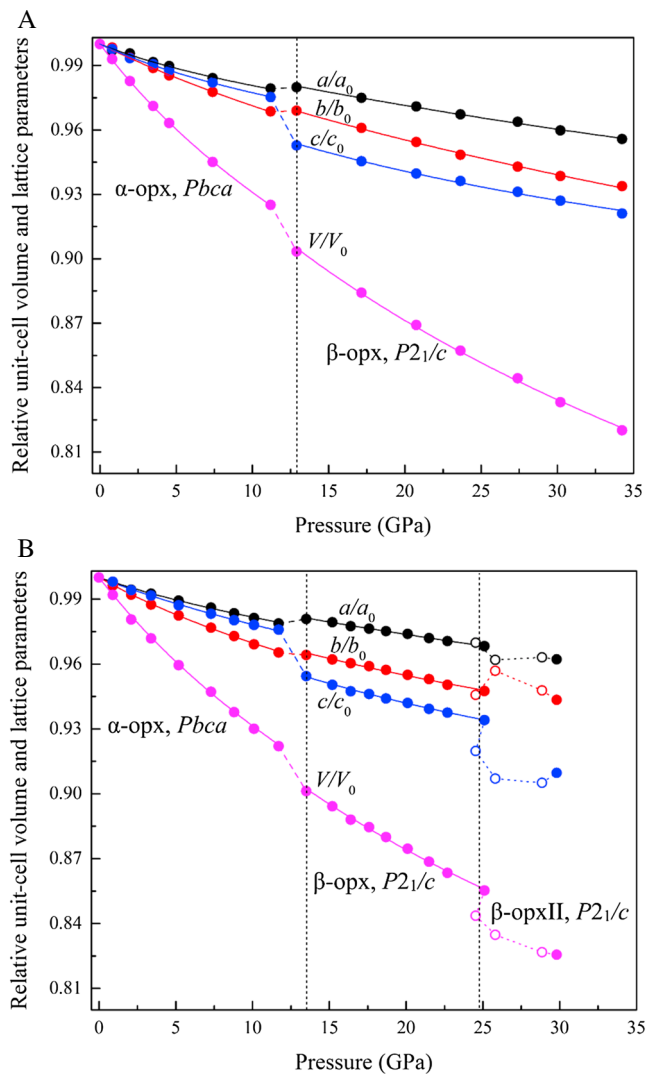


**Figure 1.** Pressure evolutions of normalized unit-cell volume and lattice parameters for (a) oEn#1 and (b) oEn#2. Data collected during decompression are indicated by open symbols. The error bars of the data points are smaller than the symbols.

oEn#1 and oEn#2 is clearly different within their experimental pressure ranges (Figures 2a and 2b). In oEn#1  $\beta$ -opx, the  $\beta$  angle continuously increases from  $92.99(3)^\circ$  to a maximum of  $94.00(3)^\circ$  at  $34.25(1)$  GPa, while oEn#2 experiences a drop of 2.9% through the  $\beta$ -opx  $\rightarrow$   $\beta$ -opxII transition (Figures 2a and 2b and Table S1).

### 3.1.4. Comparison With Previous Studies

Several earlier studies have described the pressure-induced phase transitions in synthetic Mg-end-member oEn<sub>100</sub> at ambient temperature. Serghiou et al. (2000) reported a high-pressure Raman study with single-crystal oEn<sub>100</sub> opx samples to a maximum pressure of  $\sim 70$  GPa, and two pronounced structure changes were detected at pressures between 7 and 15 GPa and between  $\sim 38$  and 40 GPa. In addition, combined powder X-ray diffraction and Raman spectroscopy high-pressure experiments on oEn<sub>100</sub> up to  $\sim 22$  GPa conducted by Lin et al. (2005) indicated a phase transition at  $\sim 10$  GPa. In the current study we conducted high-pressure single-crystal X-ray diffraction experiments on a synthetic oEn<sub>100</sub> (En#1) opx, and the structural refinements demonstrate that the sample underwent the  $\alpha \rightarrow \beta$  opx transition similar to behavior observed in oEn<sub>90</sub>, oEn<sub>87</sub>, and oEn<sub>16</sub> opx. No further phase transitions were detected up to  $34.25(1)$  GPa. As described by Serghiou et al. (2000) the second phase transition of oEn<sub>100</sub> opx occurred at  $\sim 40$  GPa, and the drastic change in the Raman

11.70(2) and 13.50(1) GPa, with a volume reduction of 2.3%, which is similar to the previously reported  $Pbca$  ( $\alpha$ -opx)  $\rightarrow$   $P2_1/c$  ( $\beta$ -opx) transitions of oEn#1, oEn<sub>90</sub>, oEn<sub>87</sub>, and oEn<sub>16</sub>. This phase transition was accompanied by the presence of the pseudomerohedral twinning, as described by Dera, Finkelstein, et al. (2013) in oEn<sub>16</sub> opx. The second high-pressure phase was observed at  $29.80(4)$  GPa with a volume decrease of 3.5%, and this phase was retained during decompression to  $24.53(3)$  GPa. Unlike the oEn<sub>90</sub> and oEn<sub>16</sub> opx, which exhibited the second phase transitions to orthorhombic structures (orthorhombic  $Pca2_1$  and  $Pbca$  space groups for oEn<sub>90</sub> and oEn<sub>16</sub>, respectively) at high pressures (Dera, Finkelstein, et al., 2013; Finkelstein et al., 2015), the oEn#2 underwent a monoclinic  $\rightarrow$  monoclinic transition (Table S3). We named the second high-pressure phase as  $\beta$ -opxII, because it has a structure only slightly modified, compared to  $\beta$ -opx, which is different from the  $\alpha$ -opx and  $\gamma$ -opx. The pseudomerohedral twinning introduced by the  $\beta$  phase disappeared through the second phase change, just as what happened for the monoclinic-orthorhombic transitions in oEn<sub>17</sub> and oEn<sub>90</sub> opxs (Dera, Finkelstein, et al., 2013; Finkelstein et al., 2015). The structure of the  $\beta$ -opx oEn#2 was successfully refined from the structure model of the  $\beta$ -opx oEn#1, and the results yielded a satisfactory refinement (Table S3). Similarly, the  $\beta$ -opxII structure was successfully refined from the structure model of the  $\beta$ -opx oEn#2 (see Table S3), and the refinement yielded reasonable figures of merits (Table S4).

### 3.1.3. Axial Compression Through the Phase Transitions

The axial compressibilities of oEn#1 and oEn#2 are anisotropic, and the compression behaviors of both samples are similar (Figures 1a and 1b). For the  $\alpha$ -opx phases of oEn#1 and oEn#2, the  $a$  direction is the least compressible while the  $b$  direction is the softest, which is similar to the oEn<sub>90</sub> and oEn<sub>16</sub> opx (Dera, Finkelstein, et al., 2013; Finkelstein et al., 2015). However, the  $c$  direction and the  $a$  direction experience the most and the least compression over the whole pressure range studied, respectively. After the first phase transition the  $a$  direction expands by 0.1% and 0.2% for oEn#1 and oEn#2, respectively, while the  $b$  direction expands by 0.4% and then shrinks by 0.1%. The  $c$  direction has the maximum reductions of 2.3% and 2.2% for oEn#1 and oEn#2, respectively.

After the second phase transition in oEn#2, the  $a$  direction shrinks by 0.7%, while the  $b$  direction expands by 1%, and the  $c$  direction again shows the largest reduction by 2.9%. The evolution of the monoclinic  $\beta$  angle of

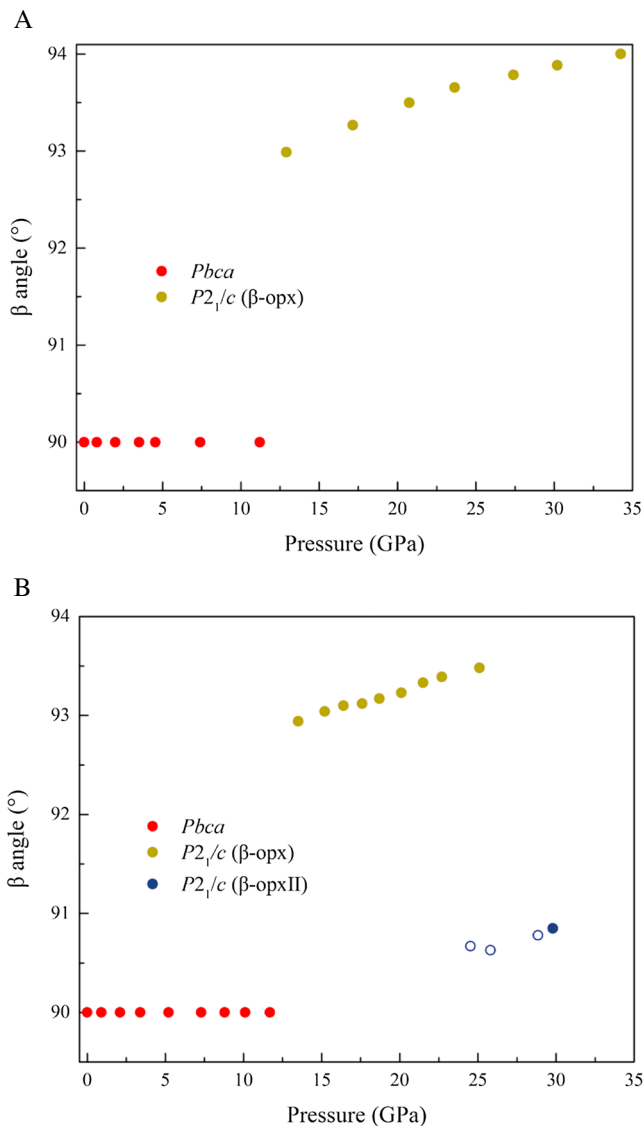


**Figure 2.** Pressure evolution of the  $\beta$  angle for (a) oEn#1 and (b) oEn#2. Data collected during decompression are indicated by open symbols. The error bars of the data points are smaller than the symbols.

spectra indicated the presence of octahedrally coordinated Si. Thus, our results on oEn#1 are generally consistent with that reported in Serghiou et al. (2000). The  $\beta$ -opx phase of oEn#1 (619 ppm water) occurs at a pressure of 12.90(2) GPa, which is within the transition pressure range (7–15 GPa) observed by Serghiou et al. (2000), but higher than reported by Lin et al. (2005). Thus, we suggest that several hundred ppm of water has insignificant effect on the transition pressure, although the pressure-transmitting media from Serghiou et al. (2000), Lin et al. (2005), and this study are different (argon, deionized water, and neon, respectively).

### 3.1.5. The $\beta$ -opx $\rightarrow$ $\beta$ -opxII Phase Transition

From previous and this experimental studies on pressure-induced metastable phase transformations on opx, it is clear that the first transition is from the  $\alpha$ -opx to  $\beta$ -opx (except for the oFs<sub>100</sub>, Hugh-Jones et al., 1996), which is the result of the tetrahedral rotation (Dera, Finkelstein, et al., 2013; Zhang et al., 2012) (Figure 3a). It is also clear that the pure Mg-oEn has no further phase transitions after the  $\beta$ -opx phase within 0–30 GPa, as indicated by high-pressure single-crystal X-ray diffraction (this study) and Raman spectroscopy (Serghiou et al., 2000). However, opx containing transition metal cations (Fe or Ni) undergoes a second phase transition after the  $\beta$ -opx at the pressures lower than 30 GPa. Similar to the  $\alpha \rightarrow \beta$  opx transition, this phase change involves mainly tetrahedral rotation (Dera, Finkelstein, et al., 2013) (as shown in  $\beta$ -opxII, Figure 3b), although Finkelstein et al. (2015) suggested that the coordination number of Si was partially increased to V in the  $\alpha$ -popx structure.

It should be noted that the second high-pressure phases ( $\alpha$ -popx and  $\gamma$ -opx) of the Fe-bearing opx including oEn<sub>16</sub> and oEn<sub>90</sub> have orthorhombic symmetries, while the  $\beta$ -opxII is monoclinic (Table 1), although the  $\beta$  angle is very close to 90°. This result indicates that the effects of Ni<sup>2+</sup> and Fe<sup>2+</sup> on the symmetry of high-pressure opx phases are different. Indeed, Ni<sup>2+</sup> and Fe<sup>2+</sup> show differences in many aspects of crystal chemistry. Fe-end-member opx is a naturally occurring mineral, whereas the (Ni, Mg)SiO<sub>3</sub> cannot be synthesized with more than 50 mol % Ni (Schwab, 1968). In the FeSiO<sub>3</sub>-MgSiO<sub>3</sub> opx systems, Fe<sup>2+</sup> is strongly enriched in the M2 site (e.g., Dera, Finkelstein, et al., 2013; Nestola et al., 2008; Zhang et al., 2011, 2012), while Ni<sup>2+</sup> shows slight preference for M1 site (Burns, 1970), and in our samples Ni<sup>2+</sup> was distributed nearly equally between the M1 and M2 sites (Table S2). The stability of the monoclinic  $\beta$ -opxII phase observed in Ni-bearing oEn#2 at high

pressures could be interpreted by crystal field theory. In an octahedral crystal field Ni<sup>2+</sup> is energetically more stable than any other high-spin divalent 3-d transition metal cation, because of its electronic configuration (Burns, 1970).

Although natural opx in mantle xenoliths are normally poor in Ni content (e.g., Ishimaru et al., 2006; Yamamoto, Hirano, et al., 2009; Yamamoto, Nakai, et al., 2009; Yamamoto et al., 2012), Ni could be enriched in opx at some particular geological conditions of the Earth's interior (Ishimaru & Arai, 2008). Experimental studies on Ni partitioning between peridotite and melt have proven that Ni can be enriched in opx and olivine at high pressures (Burns, 1973). Therefore, the discovery of the  $\beta$ -opxII adds one more piece of information to our understanding of Ni-bearing silicates at deep Earth conditions.

## 3.2. Equation of State

### 3.2.1. Equation of State at Ambient Temperature

The third-order Birch-Murnaghan equations of state (BM3 EoS) was fit to the  $P$ - $V$  curves of oEn#1 and oEn#2 using the EoSFit7c program (Angel et al., 2014; Figures 4a and 4b). The EoS parameters of oEn#1 and oEn#2

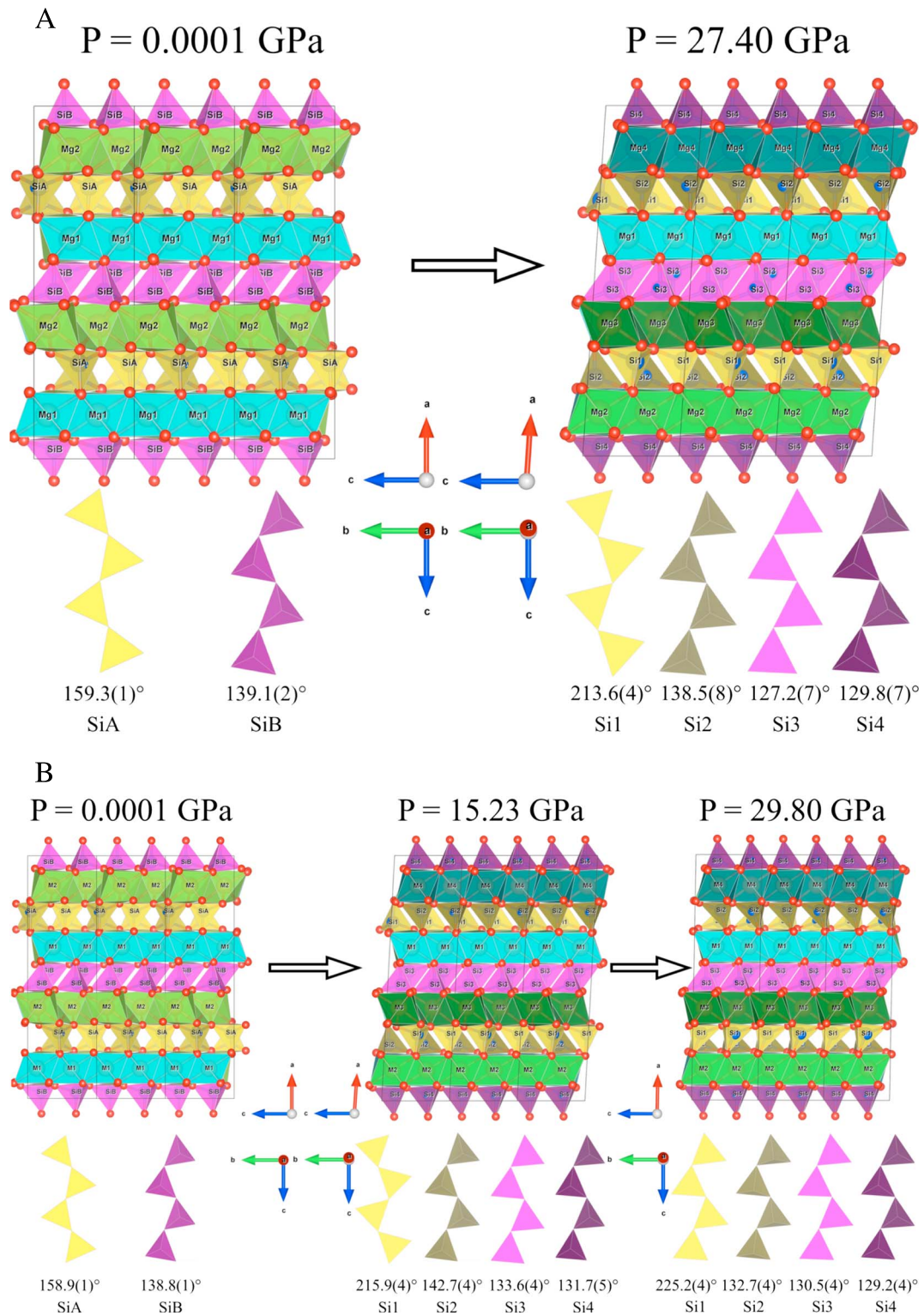


**Figure 3.** Comparison of crystal structures of high-pressure metastable phases for (a) oEn#1 and (b) oEn#2.

are consistent with previous reports (Table 2). For the  $\alpha$ -opx phase, the isothermal bulk modulus ( $K_0$ ) and its pressure derivative ( $K'_0$ ) of the pure Mg-end-member (En#1) in this study are very close to the results reported by Angel and Jackson (2002) and Periotto et al. (2012). However, the  $K_0$  values derived from Zhao et al. (1995)



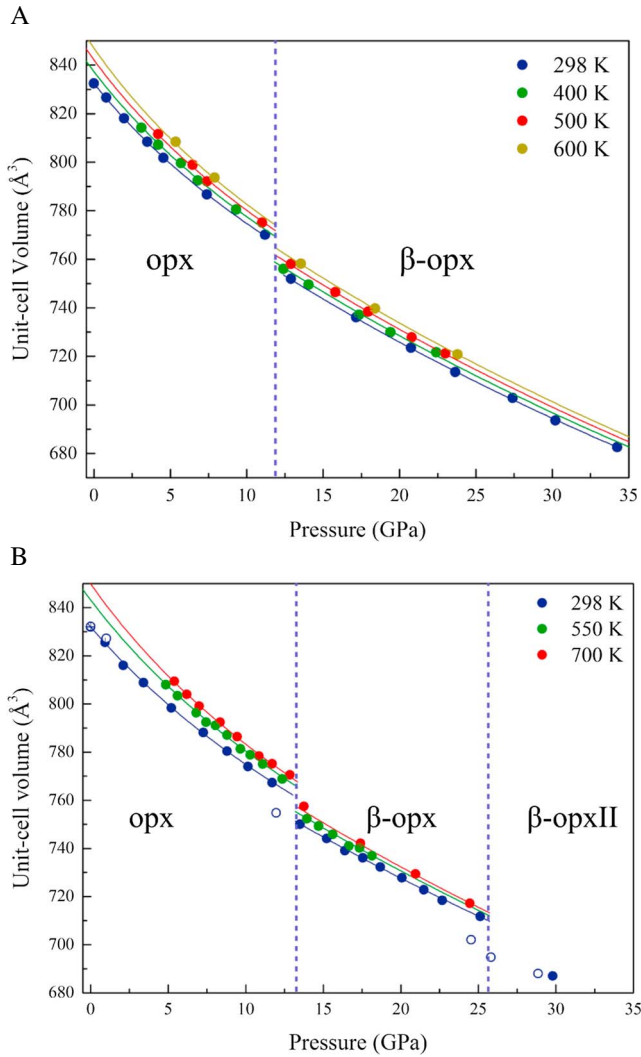


**Figure 4.** Unit cell volume of (a) oEn#1 and (b) oEn#2 as a function of pressure and temperature. Data collected during decompression are indicated by open symbols. The error bars of the data points are smaller than the symbols.

are clearly lower, probably because of the narrower experimental pressure range (0–5 GPa). For both the  $\alpha$ -opx and  $\beta$ -opx phases, the Ni-bearing oEn#2 has significantly higher  $K_0$  values than that of oEn#1. For isostructural minerals, one containing larger metal cations usually has a lower  $K_0$  (Anderson & Anderson, 1970), and  $\text{Ni}^{2+}$  has a smaller ionic radius than  $\text{Mg}^{2+}$  (Shannon, 1976). All of the oEn<sub>100</sub> samples used in studies from Zhao et al. (1995), Angel and Jackson (2002), and Periotto et al. (2012) were crystallized from a melt in the system  $\text{MgO-SiO}_2$ -lithiumvanadomolybdate at ambient pressure (Ito, 1975) and were likely free of water. Hence, we conclude that the influence of several hundred ppm of water on isothermal bulk modulus of oEn is small and comparable to that described in diopside and cEn (Gavrilenko et al., 2010; Jacobsen et al., 2010) and less pronounced than the variations accompanying changes in the major element chemistry (e.g., substitution of Mg for Ni).

The incorporation of Ni also affects the axial compression behavior of the  $\alpha$ -opx phase. The linear moduli of  $a$ ,  $b$ , and  $c$  for oEn#1 and oEn#2 were also calculated using the linear BM3 equation and EoSFit7c program. The compressibilities ( $\beta$ ) (Angel, 2000) of each axis were calculated (Table 3) yielding  $\beta_a:\beta_b:\beta_c = 1:1.25:1.21$  and  $1:1.67:1.13$  for oEn#1 and oEn#2, respectively. The incorporation of Ni clearly increases the compression anisotropy of  $\alpha$ -opx phase of oEn (Figures 1a and 1b and Table 3).

### 3.2.2. Thermal Equation of State

The unit-cell volume data (Table S1) of oEn#1 and oEn#2 measured at high pressures and temperatures were also used for subsequent thermal EoS calculations. The high-temperature Birch-Murnaghan equation was used to fit the  $P$ - $V$ - $T$  data, which is given by the following form:

$$P = (3/2)K_{T0} \left[ (V_{T0}/V)^{7/3} - (V_{T0}/V)^{5/3} \right] \times \left\{ 1 + (3/4)(K'_{T0} - 4) \left[ (V_{T0}/V)^{2/3} - 1 \right] \right\}, \quad (1)$$

where  $K_{T0}$ ,  $K'_{T0}$ , and  $V_{T0}$  are bulk modulus, its pressure derivative, and the unit cell volume at ambient pressure and temperature (in Kelvin). The effects of temperature on  $K_{T0}$  and  $V_{T0}$  are expressed as follows:

$$V_{T0} = V_0 \exp \int_{300}^T \alpha_T dT \quad (2)$$

$$K_{T0} = K_0 + (\partial K_0 / \partial T)_P \times (T - 298) \quad (3)$$

$$\alpha_T = \alpha_0 \quad (4)$$

where  $(\partial K_0 / \partial T)_P$  and  $\alpha_T$  are the temperature derivative of the bulk modulus and the volumetric thermal expansion at ambient pressure. In general, thermal expansion changes with temperature. However, in view of the relatively low experimental temperature range and the limited high-pressure and temperature data in this study,  $\alpha_T$  is often assumed to be constant over the temperature range, that is,  $\alpha_T = \alpha_0$  (e.g., Fan et al., 2015, 2017; Nishihara et al., 2003; Xu et al., 2016). The  $V_0$ ,  $K_{T0}$ , and  $K'_{T0}$  values obtained by fitting the  $P$ - $V$ - $T$  data are in agreement with EoS fit at ambient temperature within the uncertainty (Table 2).

Compared to the  $K_{T0}$  of oEn, which is significantly influenced by the incorporation Ni, the thermal expansion coefficients ( $\alpha_T$ ) of oEn#1 and oEn#2 for both phases are very comparable (Table 2). Previous thermal expansion studies on synthetic oEn<sub>100</sub> (with no analysis of water content) show a large variation range of  $\alpha_T$

**Table 3**  
Linear BM3 Fitting Parameters and Axial Compressibilities of the Lattice Parameters *a*, *b*, and *c* for the Initial PbcA Phases of oEn#1 and oEn#2

oEn#1	<i>a</i>	<i>b</i>	<i>c</i>
<i>M</i> <sub>0</sub> (GPa)	351(30)	289(12)	297(13)
<i>M'</i> <sub>0</sub>	42(13)	12(3)	36(6)
<i>β</i> <sub>0</sub> (GPa <sup>-1</sup> )	0.0028(2)	0.0035(1)	0.0034(2)
oEn#2	<i>a</i>	<i>b</i>	<i>c</i>
<i>M</i> <sub>0</sub> (GPa)	415(14)	251(5)	369(17)
<i>M'</i> <sub>0</sub>	30(5)	17(2)	19(5)
<i>β</i> <sub>0</sub> (GPa <sup>-1</sup> )	0.0024(1)	0.0040(1)	0.0027 (1)

( $2.4\text{--}4.23 \times 10^{-5} \text{ K}^{-1}$ ) (e.g., Hugh-Jones, 1997; Yang & Ghose, 1994, 1995; Yang & Prewitt, 2000; Zhao et al., 1995), all are lower than the values we obtained ( $5.7(10)$  and  $5.3(4) \times 10^{-5} \text{ K}^{-1}$ ; Table 2). In summary, oEn#1 and oEn#2, which have comparable estimated water contents, are very close in thermal expansion coefficients. Their  $\alpha_T$  values are significantly larger than reported in previous studies on synthetic oEn<sub>100</sub>, which is most likely a consequence of the incorporation of water, because water is known to enhance thermal expansion in olivine and pyrope (e.g., Fan et al., 2017; Suzuki et al., 1980; Trots et al., 2012; Ye et al., 2009). We conclude that the bulk modulus  $K_{T0}$  of oEn is more sensitive to the variation of Ni content, while the thermal expansion  $\alpha_T$  changes in response to variations in the water content.

## 4. Implications

### 4.1. The Phase Relations of MgSiO<sub>3</sub>

oEn is the second most abundant mineral in harzburgite, and its equilibrium phase boundaries have been well constrained by laboratory experiments above 1000 K. Recent experimental study suggested that oEn transforms to cEn (C2/c space group) at 7.28(9) GPa and >1000 K, and at higher pressures this phase transition requires higher temperatures (Akashi et al., 2009). Under high pressures within transition zone depths, transformations of cEn→majorite garnet and cEn→wadsleyite + stishovite are kinetically inhibited at low temperatures. These two transformations on a laboratory timescale require comparable temperature conditions (at least 1800 K) (Hogrefe et al., 1994; Nishi et al., 2008; Van Mierlo et al., 2013). At ~21 GPa and moderate temperatures (above 1500 K), cEn rapidly transforms to akimotoite (Hogrefe et al., 1994). At extremely low temperatures (below 1000 K) within the coldest part of old slabs, however, there are limited experimental studies on the oEn phase transitions (Figure 5).

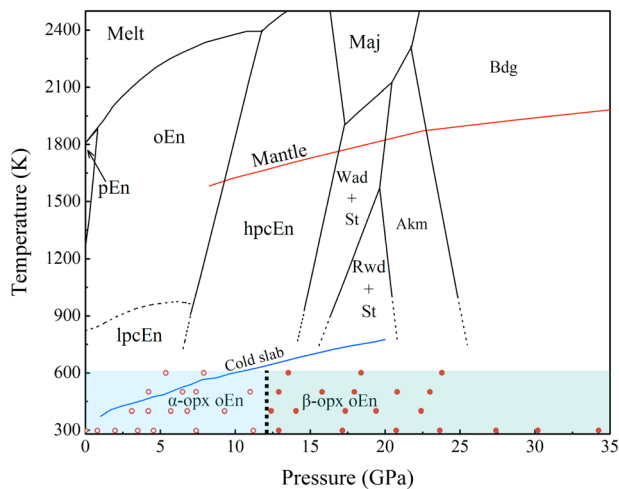


**Figure 5.** The phase relations of MgSiO<sub>3</sub> system and the results of this study. The metastable region of oEn is colored, and the open symbols and solid symbols represent stability of  $\alpha$ -opx oEn and  $\beta$ -opx oEn, respectively. This Figure is modified after Finkelstein et al. (2015). The source data include the phase diagram of MgSiO<sub>3</sub> (Fei & Bertka, 1999; Presnall, 1995), the normal mantle (Brown & Shankland, 1981), and cold slab (Bina & Navrotsky, 2000) geotherms. Note that the cold slab geotherm from Bina and Navrotsky (2000) represent the coldest part of the old and fast slabs. oEn = orthoenstatite; pen = protoenstatite; lpcen = low-pressure clinoenstatite; hpcen = high-pressure clinoenstatite; Maj = majorite garnet; Wad = wadsleyite; St = stishovite; Rwd = ringwoodite; Akm = akimotoite; Bdg = bridgmanite.

At 700 K, our experiments suggest that oEn could be metastably retained to a maximum pressure of ~13 GPa (~400 km depth), where it transforms to the  $\beta$ -opx phase, which survives at least to ~34 GPa. Geophysical models suggested that the mantle of different regions has different thermal structures (e.g., Dalton et al., 2014), and the temperature in the center of the slab at 600 km depth ranges from 900 to 1600 K (Frohlich, 1994; King et al., 2015; Kirby et al., 1996). At temperatures higher than 1000 K, the metastable  $\beta$ -opx phase is not expected within downgoing slabs, due to the oEn to cEn transformation (Akashi et al., 2009). On the other hand, extremely low temperatures (below 1000 K) are believed to be preserved within the coldest part of the old and rapid slabs (Bina & Navrotsky, 2000; Frohlich, 1994; King et al., 2015; Kirby et al., 1996). Our experiments suggest that the  $\alpha$ - to  $\beta$ -opx transition is most likely expected to occur in the harzburgite layer of a cold and old slab, which is not only the coldest part in the slab (Ganguly et al., 2009) but also contains up to 40 vol % oEn.

We estimated whether this metastable phase can be preserved over geologic time based on the following assumptions: (1) above 1000 K temperatures, the  $\beta$ -opx phase is unstable, because oEn to cEn and cEn to akimotoite transitions proceed rapidly on laboratory timescale (Akashi et al., 2009; Hogrefe et al., 1994); (2) in a cold and old slab, extremely low temperatures (below 1000 K) can be retained to a maximum depth of 600 km (Frohlich, 1994; King et al., 2015; Kirby et al., 1996); (3) the lifetime of the  $\beta$ -opx phase depends on how much time the slab requires to pass through the depth range of 400–600 km. We adopted an old and rapidly subducting slab model (the rate is 14 cm/year and the dip is 60°, Bina and Navrotsky

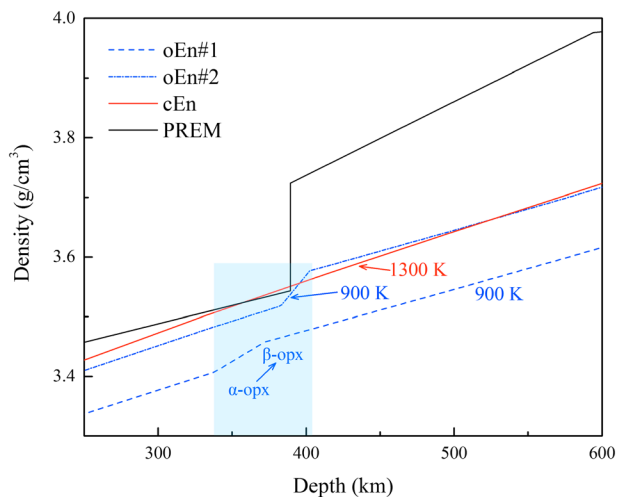


**Figure 6.** Calculated density profiles of orthoenstatite (oEn#1 and oEn#2) and clinoenstatite (cEn) along 900 and 1300 K and comparison with the PREM (Dziewonski & Anderson, 1981). Data of oEn and its high-pressure phase are from this study, while cEn data are from Shinmei et al. (1999). PREM = preliminary reference Earth model.

(2000)) for the estimation, and the results suggest that the slab requires 1.65 Myr to pass through 400–600 km depth range. Considering other factors like latent heat-induced temperature increase (Kirby et al., 1996), we concluded that the lifetime of metastable  $\beta$ -opx phase should be less than 1.65 Myr.

#### 4.2. Possible Relevance of Deep-Focus Earthquakes to the Metastable Phase Transitions of oEn

Deep earthquakes, whose hypocenter depths are greater than  $\sim 70$  km (Frohlich, 1989) and constitute a large portion of all earthquakes, are often associated with subduction zones. A prominent feature of the deep earthquakes is the depth distribution, which decays exponentially down to  $\sim 400$  km, then increases till  $\sim 600$  km, and then terminates abruptly at about 690 km (Frohlich, 1989). One of the key factors that significantly influence the deep-focus earthquakes is temperature (e.g., Frohlich, 2006; Zhan, 2017). Indeed, about two thirds of all deep-focus earthquakes (hypocenter depths greater than  $\sim 350$  km) occur in the Tonga-Kermadec region, which contains a well-known cold slab (Frohlich, 2006). However, the real mechanism of deep-focus earthquakes is still under debate (e.g., Frohlich, 1989; Green & Houston, 1995; Wang et al., 2017). Proposed mechanisms include dehydration embrittlement (e.g., Leclère et al., 2016; Peacock, 2001), thermal shear instability (e.g., Karato et al., 2001), transformational faulting (e.g., Kirby et al., 1991), and differential volume reduction between the basalt and harzburgite layers of the subducting slab (Liu & Zhang, 2015). Deep-focus earthquakes have been interpreted in terms of transformational faulting, which originates from metastable phase transition of olivine (e.g., Green & Houston, 1995; Green et al., 1990; Kirby et al., 1991), although different scenarios were considered (e.g., Karato et al., 2001; Koper et al., 1998).

The metastable phase transitions of olivine have been treated as the most likely trigger of deep-focus earthquakes because olivine is the most abundant mineral of the oceanic lithosphere and has phase transitions within this depth range (Houston, 2015). This study of metastable phase transition of oEn at temperatures below 1000 K suggests that the  $\alpha$ - to  $\beta$ -opx transition occurs around  $\sim 13$  GPa (corresponding to  $\sim 400$  km depth) accompanied by volume reductions of  $\sim 2$ –4%, also within the depth range of deep-focus earthquakes. Therefore, in an extremely cold (below 1000 K) part of an old and fast slab, the  $\alpha$ - to  $\beta$ -opx transition of oEn might be an option to enhance the transformational faulting mechanism for earthquakes around the 400 km depth.

The metastable phase transitions of olivine have been treated as the most likely trigger of deep-focus earthquakes because olivine is the most abundant mineral of the oceanic lithosphere and has phase transitions within this depth range (Houston, 2015). This study of metastable phase transition of oEn at temperatures below 1000 K suggests that the  $\alpha$ - to  $\beta$ -opx transition occurs around  $\sim 13$  GPa (corresponding to  $\sim 400$  km depth) accompanied by volume reductions of  $\sim 2$ –4%, also within the depth range of deep-focus earthquakes. Therefore, in an extremely cold (below 1000 K) part of an old and fast slab, the  $\alpha$ - to  $\beta$ -opx transition of oEn might be an option to enhance the transformational faulting mechanism for earthquakes around the 400 km depth.

#### 4.3. Metastable oEn and Stagnation of Cold Subducted Slabs

We calculated the density of oEn along 900 and 1300 K temperature utilizing the thermal equation of state parameters of oEn and its  $\beta$ -opx phase obtained in this study and the high-temperature third-order Birch-Murnaghan equation (formulas (1)–(4)), and the results were compared with the preliminary reference Earth model (PREM, Dziewonski & Anderson, 1981) density model (Figure 6). The 900 K temperature represents the coldest part of harzburgite layer of a cold slab (e.g., Tonga slab, King et al. (2015)), where the  $\alpha$ - to  $\beta$ -opx transition of oEn is expected, and 1300 K represents a hot slab (e.g., central Chile, King et al. (2015)). At 1300 K, cEn instead of oEn is the stable phase below  $\sim 250$  km (Akashi et al., 2009), and on the laboratory timescale cEn could be preserved to 21 GPa because cEn  $\rightarrow$  majorite garnet and cEn  $\rightarrow$  wadsleyite + stishovite reaction would be kinetically inhibited at this temperature (Hogrefe et al., 1994). Therefore, at 1300 K, oEn in the harzburgite layer likely transforms to cEn before the slab sinks into the transition zone, and the metastable  $\alpha$ - to  $\beta$ -opx phase transition is not expected.

The extremely low temperature (below 1000 K) could be retained within the coldest part of the old and fast slabs to a maximum depth of 600 km (Frohlich, 1994; King et al., 2015; Kirby et al., 1996). Based on our study, oEn is expected to be metastably preserved to such a depth within the harzburgite layer. As is shown in Figure 6, oEn#2 is denser than oEn#1 by  $\sim 3\%$  at 600 km. Compared with the PREM density model, both oEn#s have notably smaller densities, even if one accounts for the density jump induced by the  $\alpha$ - to  $\beta$ -opx

transition, and the PREM model is ~9% denser than oEn#1 at 600 km. Geophysical models suggested that the temperature of stagnant slabs in the lower transition zone can be as low as 900 K in regions such as North Honshu and Tonga (King et al., 2015). Therefore, the existence of the low-density metastable oEn increases the buoyant force of the subducted slab and may slowdown the subduction rate and contribute to the slab stagnation in the transition zone. It should be noted that the effect of metastable oEn and its  $\beta$ -opx phase could be limited to the coldest part of the old and rapidly subducted slabs (e.g., Tonga slab, Fukao and Obayashi (2013)).

## 5. Conclusions

We have investigated the metastable phase transitions of two orthoenstatite samples (oEn#1 and oEn#2) at high pressures and temperatures to ~34 GPa and 700 K. The pure Mg-end-member oEn#1 undergoes the  $\alpha \rightarrow \beta$ -opx transition and retains the  $\beta$ -opx structure to ~34 GPa, while the Ni-bearing oEn#2 experiences a further transition at ~30 GPa. The presence of the new monoclinic  $\beta$ -opxII phase can be interpreted by the higher crystal field stabilization energy of  $\text{Ni}^{2+}$ , compared to  $\text{Fe}^{2+}$ . The incorporation of several hundred ppm water has negligible effects on the bulk modulus of oEn but could significantly alter the thermal expansion. On the contrary, the incorporation of Ni could increase the bulk modulus but has negligible effects on thermal expansion. The metastable phase transitions of oEn may be relevant to the deep earthquakes in the cold subduction zones and contribute to the deep-focus earthquakes occurring at depths around 400 km depth. In a cold subduction zone, the presence of metastable oEn could promote the slab stagnation above the 660 km discontinuity.

### Acknowledgments

This project was supported by the National Natural Science Foundation of China (grant 41772043), the Joint Research Fund in Huge Scientific Equipment (U1632112) under cooperative agreement between NSFC and CAS, the Chinese Academy of Sciences "Light of West China" Program (Dawei Fan, 2017), Youth Innovation Promotion Association CAS (Dawei Fan, 2018), the Strategic Priority Research Program (B) of the Chinese Academy of Sciences (XDB 18010401), the CPSF-CAS Joint Foundation for Excellent Postdoctoral Fellows (grant 2017LH014), and the National Science Foundation under grants EAR1344942 and EAR1722969. This work was performed at GeoSoilEnviroCARS (Sector 13), Partnership for Extreme Crystallography program (PX<sup>2</sup>), Advanced Photon Source (APS), and Argonne National Laboratory. GeoSoilEnviroCARS is supported by the National Science Foundation—Earth Sciences (EAR-1128799) and Department of Energy Geosciences (DE-FG02-94ER14466). PX<sup>2</sup> program is supported by COMPRES under NSF Cooperative Agreement EAR 11-57758. The use of the COMPRES-GSECARS gas loading system was supported by COMPRES under NSF Cooperative Agreement EAR 11-57758 and by GSECARS. Development of the ATREX software used for data analysis is supported by NSF grant EAR1440005. The use of the Advanced Photon Source was supported by the U.S. Department of Energy, Office of Science, Office of Basic Energy Sciences, under contract DE-AC02-06CH11357. We would like to thank two anonymous reviewers for their thorough and helpful comments, which helped to improve the quality of this manuscript, and Michael Walter for handling this manuscript. Readers can access the additional data in the supporting information.

### References

- Agrusta, R., Hunen, J., & Goes, S. (2014). The effect of metastable pyroxene on the slab dynamics. *Geophysical Research Letters*, *41*, 8800–8808. <https://doi.org/10.1002/2014GL062159>
- Akashi, A., Nishihara, Y., Takahashi, E., Nakajima, Y., Tange, Y., & Funakoshi, K. (2009). Orthoenstatite/clinoenstatite phase transformation in  $\text{MgSiO}_3$  at high-pressure and high-temperature determined by in situ X-ray diffraction: Implications for nature of the X discontinuity. *Journal of Geophysical Research*, *114*, B04206. <https://doi.org/10.1029/2008JB005894>
- Akins, J. A., Luo, S. N., Asimow, P. D., & Ahrens, T. J. (2004). Shock-induced melting of  $\text{MgSiO}_3$  perovskite and implications for melts in Earth's lowermost mantle. *Geophysical Research Letters*, *31*, L14612. <https://doi.org/10.1029/2004GL020237>
- Anderson, D. L. (1989). *Theory of the Earth*. Boston, MA: Blackwell Scientific Publications.
- Anderson, D. L., & Anderson, O. L. (1970). Bulk modulus-volume relationship for oxides. *Journal of Geophysical Research*, *75*(17), 3494–3500. <https://doi.org/10.1029/JB075i017p03494>
- Angel, R. J. (2000). Equations of state. *Reviews in Mineralogy and Geochemistry*, *41*(1), 35–59.
- Angel, R. J., Gonzalez-Platas, J., & Alvaro, M. (2014). EosFit7c and a Fortran module (library) for equation of state calculations. *Zeitschrift für Kristallographie-Crystalline Materials*, *229*(5), 405–419.
- Angel, R. J., & Jackson, J. M. (2002). Elasticity and equation of state of orthoenstatite,  $\text{MgSiO}_3$ . *American Mineralogist*, *87*(4), 558–561. <https://doi.org/10.2138/am-2002-0419>
- Aubaud, C., Hauri, E. H., & Hirschmann, M. M. (2004). Hydrogen partition coefficients between nominally anhydrous minerals and basaltic melts. *Geophysical Research Letters*, *31*, L20611. <https://doi.org/10.1029/2004GL021341>
- Bell, D. R., Ihinger, P. D., & Rossman, G. R. (1995). Quantitative analysis of trace OH in garnet and pyroxenes. *American Mineralogist*, *80*(5-6), 465–474. <https://doi.org/10.2138/am-1995-5-607>
- Bina, C. R. (2013). Mineralogy: Garnet goes hungry. *Nature Geoscience*, *6*(5), 335–336. <https://doi.org/10.1038/ngeo1804>
- Bina, C. R., & Navrotsky, A. (2000). Possible presence of high-pressure ice in cold subducting slabs. *Nature*, *408*(6814), 844–847. <https://doi.org/10.1038/35048555>
- Bina, C. R., Stein, S., Marton, F. C., & Van Ark, E. M. (2001). Implications of slab mineralogy for subduction dynamics. *Physics of the Earth and Planetary Interiors*, *127*(1-4), 51–66. [https://doi.org/10.1016/S0031-9201\(01\)00221-7](https://doi.org/10.1016/S0031-9201(01)00221-7)
- Brown, J., & Shankland, T. (1981). Thermodynamic parameters in the Earth as determined from seismic profiles. *Geophysical Journal International*, *66*(3), 579–596. <https://doi.org/10.1111/j.1365-246X.1981.tb04891.x>
- Burns, R. G. (1970). Site preferences of transition metal ions in silicate crystal structures. *Chemical Geology*, *5*(4), 275–283. [https://doi.org/10.1016/0009-2541\(70\)90045-8](https://doi.org/10.1016/0009-2541(70)90045-8)
- Burns, R. G. (1973). The partitioning of trace transition elements in crystal structures: A provocative review with applications to mantle geochemistry. *Geochimica et Cosmochimica Acta*, *37*(11), 2395–2403. [https://doi.org/10.1016/0016-7037\(73\)90287-1](https://doi.org/10.1016/0016-7037(73)90287-1)
- Chang, Y.-Y., Hsieh, W.-P., Tan, E., & Chen, J. (2017). Hydration-reduced lattice thermal conductivity of olivine in Earth's upper mantle. *Proceedings of the National Academy of Sciences of the United States of America*, *114*(16), 4078–4081. <https://doi.org/10.1073/pnas.1616216114>
- Dalton, C. A., Langmuir, C. H., & Gale, A. (2014). Geophysical and geochemical evidence for deep temperature variations beneath mid-ocean ridges. *Science*, *344*(6179), 80–83. <https://doi.org/10.1126/science.1249466>
- Dera, P., Finkelstein, G. J., Duffy, T. S., Downs, R. T., Meng, Y., Prakapenka, V., & Tkachev, S. (2013). Metastable high-pressure transformations of orthoferrosilite  $\text{Fs}_{82}$ . *Physics of the Earth and Planetary Interiors*, *221*, 15–21. <https://doi.org/10.1016/j.pepi.2013.06.006>
- Dera, P., Zhuravlev, K., Prakapenka, V., Rivers, M. L., Finkelstein, G. J., Grubor-Urošević, O., et al. (2013). High pressure single-crystal micro X-ray diffraction analysis with GSE\_ADA/RSV software. *High Pressure Research*, *33*(3), 466–484. <https://doi.org/10.1080/08957959.2013.806504>

- Dolomanov, O. V., Bourhis, L. J., Gildea, R. J., Howard, J. A., & Puschmann, H. (2009). OLEX2: A complete structure solution, refinement and analysis program. *Journal of Applied Crystallography*, 42(2), 339–341. <https://doi.org/10.1107/S0021889808042726>
- Dziewonski, A. M., & Anderson, D. L. (1981). Preliminary reference Earth model. *Physics of the Earth and Planetary Interiors*, 25(4), 297–356. [https://doi.org/10.1016/0031-9201\(81\)90046-7](https://doi.org/10.1016/0031-9201(81)90046-7)
- Fan, D., Lu, C., Xu, J., Yan, B., Yang, B., & Chen, J. (2017). Effects of water on P-V-T equation of state of pyrope. *Physics of the Earth and Planetary Interiors*, 267, 9–18. <https://doi.org/10.1016/j.pepi.2017.03.005>
- Fan, D., Ma, M., Wei, S., Chen, Z., & Xie, H. (2013). High pressure elastic behavior of synthetic  $Mg_3Y_2(SiO_4)_3$  garnet up to 9 GPa. *Advances in Materials Science and Engineering*, 2013, 502702.
- Fan, D., Xu, J., Ma, M., Wei, S., Zhang, B., Liu, J., & Xie, H. (2015). P-V-T equation of state of  $Ca_3Cr_2Si_3O_{12}$  uvarovite garnet by using a diamond-anvil cell and in-situ synchrotron X-ray diffraction. *American Mineralogist*, 100(2–3), 588–597.
- Farrugia, L. J. (2012). WinGX and ORTEP for windows: An update. *Applied Crystallography*, 45(4), 849–854. <https://doi.org/10.1107/S0021889812029111>
- Fei, Y., & Bertka, C. M. (1999). Phase transitions in the Earth's mantle and mantle petrology. In Y. Fei, C. M. Bertka, & B. O. Mysen (Eds.), *Mantle Petrology: Field observations and high pressure experimentation* (pp. 189–207). Houston, TX: Geochemical Society.
- Fei, Y., Ricolleau, A., Frank, M., Mibe, K., Shen, G., & Prakapenka, V. (2007). Toward an internally consistent pressure scale. *Proceedings of the National Academy of Sciences of the United States of America*, 104(22), 9182–9186. <https://doi.org/10.1073/pnas.0609013104>
- Finkelstein, G. J., Dera, P. K., & Duffy, T. S. (2015). Phase transitions in orthopyroxene ( $En_{90}$ ) to 49 GPa from single-crystal X-ray diffraction. *Physics of the Earth and Planetary Interiors*, 244, 78–86. <https://doi.org/10.1016/j.pepi.2014.10.009>
- Frohlich, C. (1989). The nature of deep-focus earthquakes. *Annual Review of Earth and Planetary Sciences*, 17(1), 227–254. <https://doi.org/10.1146/annurev.ea.17.050189.001303>
- Frohlich, C. (1994). A break in the deep. *Nature*, 368(6467), 100–101. <https://doi.org/10.1038/368100a0>
- Frohlich, C. (2006). *Deep earthquakes*. Cambridge, UK: Cambridge University Press. <https://doi.org/10.1017/CBO9781107297562>
- Frost, D. J. (2008). The upper mantle and transition zone. *Elements*, 4(3), 171–176. <https://doi.org/10.2113/GSELEMENTS.4.3.171>
- Frost, D. J., & Dolejš, D. (2007). Experimental determination of the effect of  $H_2O$  on the 410-km seismic discontinuity. *Earth and Planetary Science Letters*, 256(1–2), 182–195. <https://doi.org/10.1016/j.epsl.2007.01.023>
- Fu, H., & Zhu, C. (1980). Testing parameters such as temperature, pressure in static super high pressure apparatus. *Physics*, 9(3), 193–195.
- Fukao, Y., & Obayashi, M. (2013). Subducted slabs stagnant above, penetrating through, and trapped below the 660 km discontinuity. *Journal of Geophysical Research: Solid Earth*, 118, 5920–5938. <https://doi.org/10.1002/2013JB010466>
- Ganguly, J., Freed, A. M., & Saxena, S. K. (2009). Density profiles of oceanic slabs and surrounding mantle: Integrated thermodynamic and thermal modeling, and implications for the fate of slabs at the 660 km discontinuity. *Physics of the Earth and Planetary Interiors*, 172(3–4), 257–267. <https://doi.org/10.1016/j.pepi.2008.10.005>
- Gavrilenko, P., Ballaran, T. B., & Keppler, H. (2010). The effect of Al and water on the compressibility of diopside. *American Mineralogist*, 95(4), 608–616. <https://doi.org/10.2138/am.2010.3400>
- Ghosh, S., Ohtani, E., Litasov, K. D., Suzuki, A., Dobson, D., & Funakoshi, K. (2013). Effect of water in depleted mantle on post-spinel transition and implication for 660 km seismic discontinuity. *Earth and Planetary Science Letters*, 371, 103–111.
- Green, H. W., & Houston, H. (1995). The mechanics of deep earthquakes. *Annual Review of Earth and Planetary Sciences*, 23(1), 169–213. <https://doi.org/10.1146/annurev.ea.23.050195.001125>
- Green, H. W., Young, T. E., Walker, D., & Scholz, C. H. (1990). Anticrack-associated faulting at very high pressure in natural olivine. *Nature*, 348(6303), 720–722. <https://doi.org/10.1038/348720a0>
- Hirose, K., Sinmyo, R., Sata, N., & Ohishi, Y. (2006). Determination of post-perovskite phase transition boundary in  $MgSiO_3$  using Au and MgO pressure standards. *Geophysical Research Letters*, 33, L01310. <https://doi.org/10.1029/2005GL024468>
- Hirschmann, M. M., Aubaud, C., & Withers, A. C. (2005). Storage capacity of  $H_2O$  in nominally anhydrous minerals in the upper mantle. *Earth and Planetary Science Letters*, 236(1–2), 167–181. <https://doi.org/10.1016/j.epsl.2005.04.022>
- Hogrefe, A., Rubie, D., Sharp, T., & Seifert, F. (1994). Metastability of enstatite in deep subducting lithosphere. *Nature*, 372(6504), 351–353. <https://doi.org/10.1038/372351a0>
- Houston, H. (2015). Deep earthquakes. In *Treatise on geophysics* (2nd ed., chap. 4.13, pp. 329–354). Amsterdam, Netherlands: Elsevier.
- Hugh-Jones, D. (1997). Thermal expansion of  $MgSiO_3$  and  $FeSiO_3$  ortho- and clinopyroxenes. *American Mineralogist*, 82(7–8), 689–696. <https://doi.org/10.2138/am-1997-7-806>
- Hugh-Jones, D., Sharp, T., Angel, R., & Woodland, A. (1996). The transition of orthoferrosillite to high-pressure C2/c clinoferrosillite at ambient temperature. *European Journal of Mineralogy*, 8(6), 1337–1345.
- Ishimaru, S., & Arai, S. (2008). Nickel enrichment in mantle olivine beneath a volcanic front. *Contributions to Mineralogy and Petrology*, 156(1), 119–131. <https://doi.org/10.1007/s00410-007-0277-6>
- Ishimaru, S., Arai, S., Ishida, Y., Shirasaka, M., & Okrugin, V. M. (2006). Melting and multi-stage metasomatism in the mantle wedge beneath a frontal arc inferred from highly depleted peridotite xenoliths from the Avacha volcano, southern Kamchatka. *Journal of Petrology*, 48(2), 395–433. <https://doi.org/10.1093/ptrology/egl065>
- Ito, E., & Navrotsky, A. (1985).  $MgSiO_3$  ilmenite; calorimetry, phase equilibria, and decomposition at atmospheric pressure. *American Mineralogist*, 70(9–10), 1020–1026.
- Ito, J. (1975). High temperature solvent growth of orthoenstatite,  $MgSiO_3$ , in air. *Geophysical Research Letters*, 2(12), 533–536. <https://doi.org/10.1029/GL002i012p00533>
- Jackson, J. M., Sinogeikin, S. V., Carpenter, M. A., & Bass, J. D. (2004). Novel phase transition in orthoenstatite. *American Mineralogist*, 89(1), 239–244. <https://doi.org/10.2138/am-2004-0128>
- Jacobsen, S. D. (2006). Effect of water on the equation of state of nominally anhydrous minerals. *Reviews in Mineralogy and Geochemistry*, 62(1), 321–342. <https://doi.org/10.2138/rmg.2006.62.14>
- Jacobsen, S. D., Liu, Z., Ballaran, T. B., Littlefield, E. F., Ehm, L., & Hemley, R. J. (2010). Effect of  $H_2O$  on upper mantle phase transitions in  $MgSiO_3$ : Is the depth of the seismic X-discontinuity an indicator of mantle water content? *Physics of the Earth and Planetary Interiors*, 183(1–2), 234–244. <https://doi.org/10.1016/j.pepi.2010.06.015>
- Jahn, S. (2008). High-pressure phase transitions in  $MgSiO_3$  orthoenstatite studied by atomistic computer simulation. *American Mineralogist*, 93(4), 528–532. <https://doi.org/10.2138/am.2008.2710>
- Kantor, I., Prakapenka, V., Kantor, A., Dera, P., Kurnosov, A., Sinogeikin, S., et al. (2012). BX90: A new diamond anvil cell design for X-ray diffraction and optical measurements. *Review of Scientific Instruments*, 83(12), 125102.

- Karato, S.-i., Riedel, M. R., & Yuen, D. A. (2001). Rheological structure and deformation of subducted slabs in the mantle transition zone: Implications for mantle circulation and deep earthquakes. *Physics of the Earth and Planetary Interiors*, 127(1-4), 83–108. [https://doi.org/10.1016/S0031-9201\(01\)00223-0](https://doi.org/10.1016/S0031-9201(01)00223-0)
- King, S. D., Frost, D. J., & Rubie, D. C. (2015). Why cold slabs stagnate in the transition zone. *Geology*, 43(3), 231–234. <https://doi.org/10.1130/G36320.1>
- Kirby, S., Stern, L., & Durham, W. (1991). Mantle phase changes and deep-earthquake faulting in subducting lithosphere. *Science*, 252(5003), 216–225. <https://doi.org/10.1126/science.252.5003.216>
- Kirby, S. H., Stein, S., Okal, E. A., & Rubie, D. C. (1996). Metastable mantle phase transformations and deep earthquakes in subducting oceanic lithosphere. *Reviews of Geophysics*, 34(2), 261–306. <https://doi.org/10.1029/96RG01050>
- Koper, K. D., Wiens, D. A., Dorman, L. M., Hildebrand, J. A., & Webb, S. C. (1998). Modeling the Tonga slab: Can travel time data resolve a metastable olivine wedge? *Journal of Geophysical Research*, 103(B12), 30,079–30,100. <https://doi.org/10.1029/98JB01517>
- Leclère, H., Faulkner, D., Wheeler, J., & Mariani, E. (2016). Permeability control on transient slip weakening during gypsum dehydration: Implications for earthquakes in subduction zones. *Earth and Planetary Science Letters*, 442, 1–12. <https://doi.org/10.1016/j.epsl.2016.02.015>
- Lin, C.-C. (2004). Pressure-induced polymorphism in enstatite (MgSiO<sub>3</sub>) at room temperature: Clinoenstatite and orthoenstatite. *Journal of Physics and Chemistry of Solids*, 65(5), 913–921. <https://doi.org/10.1016/j.jpcs.2003.09.028>
- Lin, C.-M., Chao, J., & Lin, C.-C. (2005). Metastable phase transition of orthoenstatite (MgSiO<sub>3</sub>) under high pressure. *Solid State Sciences*, 7(3), 293–297. <https://doi.org/10.1016/j.solidstatesciences.2004.10.005>
- Litasov, K. D., Ohtani, E., Sano, A., Suzuki, K., & Funakoshi, K. (2005). Wet subduction versus cold subduction. *Geophysical Research Letters*, 32, L13312. <https://doi.org/10.1029/2005GL022921>
- Liu, L., & Zhang, J. S. (2015). Differential contraction of subducted lithosphere layers generates deep earthquakes. *Earth and Planetary Science Letters*, 421, 98–106. <https://doi.org/10.1016/j.epsl.2015.03.053>
- Mosenfelder, J. L., Marton, F. C., Ross, C. R., Kerschhofer, L., & Rubie, D. C. (2001). Experimental constraints on the depth of olivine metastability in subducting lithosphere. *Physics of the Earth and Planetary Interiors*, 127(1-4), 165–180. [https://doi.org/10.1016/S0031-9201\(01\)00226-6](https://doi.org/10.1016/S0031-9201(01)00226-6)
- Murakami, M., Hirose, K., Kawamura, K., Sata, N., & Ohishi, Y. (2004). Post-perovskite phase transition in MgSiO<sub>3</sub>. *Science*, 304(5672), 855–858. <https://doi.org/10.1126/science.1095932>
- Murakami, T., Takéuchi, Y., & Yamanaka, T. (1982). The transition of orthoenstatite to protoenstatite and the structure at 1080 C. *Zeitschrift für Kristallographie-Crystalline Materials*, 160(3-4), 299–312. <https://doi.org/10.1524/zkri.1982.160.3-4.299>
- Nestola, F., Ballaran, T. B., Balic-Zunic, T., Secco, L., & Dal Negro, A. (2008). The high-pressure behavior of an Al- and Fe-rich natural orthopyroxene. *American Mineralogist*, 93(4), 644–652. <https://doi.org/10.2138/am.2008.2693>
- Nishi, M., Kato, T., Kubo, T., & Kikegawa, T. (2008). Survival of pyropic garnet in subducting plates. *Physics of the Earth and Planetary Interiors*, 170(3-4), 274–280. <https://doi.org/10.1016/j.pepi.2008.03.013>
- Nishi, M., Kubo, T., Ohfuji, H., Kato, T., Nishihara, Y., & Irifune, T. (2013). Slow Si-Al interdiffusion in garnet and stagnation of subducting slabs. *Earth and Planetary Science Letters*, 361, 44–49. <https://doi.org/10.1016/j.epsl.2012.11.022>
- Nishihara, Y., Takahashi, E., Matsukage, K., & Kikegawa, T. (2003). Thermal equation of state of omphacite. *American Mineralogist*, 88(1), 80–86. <https://doi.org/10.2138/am-2003-0110>
- Oganov, A. R., & Ono, S. (2004). Theoretical and experimental evidence for a post-perovskite phase of MgSiO<sub>3</sub> in Earth's D" layer. *Nature*, 430(6998), 445–448. <https://doi.org/10.1038/nature02701>
- Padrón-Navarta, J. A., Hermann, J., & O'Neill, H. S. C. (2014). Site-specific hydrogen diffusion rates in forsterite. *Earth and Planetary Science Letters*, 392, 100–112. <https://doi.org/10.1016/j.epsl.2014.01.055>
- Paterson, M. (1982). The determination of hydroxyl by infrared absorption in quartz, silicate glasses, and similar materials. *Bulletin de la Société Française de Mineralogie*, 105, 20–29.
- Peacock, S. M. (2001). Are the lower planes of double seismic zones caused by serpentine dehydration in subducting oceanic mantle? *Geology*, 29(4), 299–302. [https://doi.org/10.1130/0091-7613\(2001\)029%3C0299:ATLPOD%3E2.0.CO;2](https://doi.org/10.1130/0091-7613(2001)029%3C0299:ATLPOD%3E2.0.CO;2)
- Pearson, D., Canil, D., & Shirey, S. (2003). Mantle samples included in volcanic rocks: Xenoliths and diamonds. In H. D. Holland, & K. K. Turekian (Eds.), *The mantle and core, Treatise on Geochemistry* (Vol. 3, pp. 171–275). Amsterdam: Elsevier. <https://doi.org/10.1016/B0-08-043751-6/02005-3>
- Periotto, B., Balić-Zunić, T., Nestola, F., Katerinopoulou, A., & Angel, R. J. (2012). Re-investigation of the crystal structure of enstatite under high-pressure conditions. *American Mineralogist*, 97(10), 1741–1748. <https://doi.org/10.2138/am.2012.4157>
- Peslier, A. H., & Bizimis, M. (2015). Water in Hawaiian peridotite minerals: A case for a dry metasomatized oceanic mantle lithosphere. *Geochemistry, Geophysics, Geosystems*, 16, 1211–1232. <https://doi.org/10.1002/2015GC005780>
- Presnall, D. C. (1995). Phase diagrams of Earth-forming minerals. Mineral physics and crystallography: A handbook of physical constants. *American Geophysical Union*, 2, 248–268.
- Rauch, M., & Keppler, H. (2002). Water solubility in orthopyroxene. *Contributions to Mineralogy and Petrology*, 143(5), 525–536. <https://doi.org/10.1007/s00410-002-0365-6>
- Ringwood, A. E. (1982). Phase transformations and differentiation in subducted lithosphere: Implications for mantle dynamics, basalt petrogenesis, and crustal evolution. *The Journal of Geology*, 90(6), 611–643. <https://doi.org/10.1086/628721>
- Rivers, M., Prakapenka, V. B., Kubo, A., Pullins, C., Holl, C. M., & Jacobsen, S. D. (2008). The COMPRES/GSECARS gas-loading system for diamond anvil cells at the Advanced Photon Source. *High Pressure Research*, 28(3), 273–292. <https://doi.org/10.1080/08957950802333593>
- Schwab, R. G. (1968). Das system Mg<sub>2</sub>Si<sub>2</sub>O<sub>6</sub>-MgNiSi<sub>2</sub>O<sub>6</sub>. *New Jahrb Min Monatsch*, 337–350.
- Serghiou, G., Boehler, R., & Chopelas, A. (2000). Reversible coordination changes in crystalline silicates at high pressure and ambient temperature. *Journal of Physics: Condensed Matter*, 12(6), 849–857.
- Shan, S., Wang, R., Guo, J., & Li, H. (2007). Pressure calibration for the sample cell of YJ-3000t multi-anvil press at high-temperature and high-pressure. *Chinese Journal of High Pressure Physics*, 21, 367–372.
- Shannon, R. (1976). Revised effective ionic radii and systematic studies of interatomic distances in halides and chalcogenides. *Acta Crystallogr. Sect. A*, 32(5), 751–767. <https://doi.org/10.1107/S0567739476001551>
- Sheldrick, G. M. (2007). A short history of SHELX. *Acta Crystallogr. Sect. A*, 64(1), 112–122.
- Shinmei, T., Tomioka, N., Fujino, K., Kuroda, K., & Irifune, T. (1999). In situ X-ray diffraction study of enstatite up to 12 GPa and 1473 K and equations of state. *American Mineralogist*, 84(10), 1588–1594. <https://doi.org/10.2138/am-1999-1012>
- Smyth, J. R. (1971). Protoenstatite: A crystal-structure refinement at 1100 C. *Zeitschrift für Kristallographie-Crystalline Materials*, 134, 262–274.
- Smyth, J. R., Frost, D. J., & Nestola, F. (2005). Hydration of olivine and the Earth's deep water cycle. *Geochimica et Cosmochimica Acta*, 69, A746.
- Suzuki, I., Ohtani, E., & Kumazawa, M. (1980). Thermal expansion of modified spinel, β-Mg<sub>2</sub>SiO<sub>4</sub>. *Journal of Physics of the Earth*, 28(3), 273–280. <https://doi.org/10.4294/jpe1952.28.273>

- Trots, D. M., Kurnosov, A., Boffa Ballaran, T., & Frost, D. J. (2012). High-temperature structural behaviors of anhydrous wadsleyite and forsterite. *American Mineralogist*, *97*(10), 1582–1590. <https://doi.org/10.2138/am.2012.3992>
- Van Mierlo, W., Langenhorst, F., Frost, D., & Rubie, D. (2013). Stagnation of subducting slabs in the transition zone due to slow diffusion in majoritic garnet. *Nature Geoscience*, *6*(5), 400–403. <https://doi.org/10.1038/ngeo1772>
- Walter, M., Kohn, S., Araujo, D., Bulanova, G., Smith, C., Gaillou, E., et al. (2011). Deep mantle cycling of oceanic crust: Evidence from diamonds and their mineral inclusions. *Science*, *334*(6052), 54–57. <https://doi.org/10.1126/science.1209300>
- Wang, Y., Zhu, L., Shi, F., Schubnel, A., Hilaret, N., Yu, T., et al. (2017). A laboratory nanoseismological study on deep-focus earthquake micromechanics. *Science Advances*, *3*(7), e1601896. <https://doi.org/10.1126/sciadv.1601896>
- Warren, J. M., & Hauri, E. H. (2014). Pyroxenes as tracers of mantle water variations. *Journal of Geophysical Research: Solid Earth*, *119*, 1851–1881. <https://doi.org/10.1002/2013JB010328>
- Woodland, A. B. (1998). The orthorhombic to high-P monoclinic phase transition in Mg-Fe pyroxenes: Can it produce a seismic discontinuity? *Geophysical Research Letters*, *25*(8), 1241–1244. <https://doi.org/10.1029/98GL00857>
- Xu, J., Kuang, Y., Zhang, B., Liu, Y., Fan, D., Li, X., & Xie, H. (2016). Thermal equation of state of natural tourmaline at high pressure and temperature. *Physics and Chemistry of Minerals*, *43*(5), 315–326. <https://doi.org/10.1007/s00269-015-0796-z>
- Xu, J., Zhang, D., Dera, P., Zhang, B., & Fan, D. (2017). Experimental evidence for the survival of augite to transition zone depths, and implications for subduction zone dynamics. *American Mineralogist*, *102*(7), 1516–1524. <https://doi.org/10.2138/am-2017-5959>
- Xu, J., Zhang, D., Fan, D., Downs, R. T., Hu, Y., & Dera, P. (2017). Isosymmetric pressure-induced bonding increase changes compression behavior of clinopyroxenes across jadeite-aegirine solid solution in subduction zones. *Journal of Geophysical Research: Solid Earth*, *122*, 142–157. <https://doi.org/10.1002/2016JB013502>
- Yamamoto, J., Hirano, N., Abe, N., & Hanyu, T. (2009). Noble gas isotopic compositions of mantle xenoliths from northwestern Pacific lithosphere. *Chemical Geology*, *268*(3–4), 313–323. <https://doi.org/10.1016/j.chemgeo.2009.09.009>
- Yamamoto, J., Nakai, S. i., Nishimura, K., Kaneoka, I., Kagi, H., Sato, K., et al. (2009). Intergranular trace elements in mantle xenoliths from Russian far east: Example for mantle metasomatism by hydrous melt. *Island Arc*, *18*(1), 225–241. <https://doi.org/10.1111/j.1440-1738.2008.00642.x>
- Yamamoto, J., Nishimura, K., Ishibashi, H., Kagi, H., Arai, S., & Prikhod'ko, V. S. (2012). Thermal structure beneath far eastern Russia inferred from geothermobarometric analyses of mantle xenoliths: Direct evidence for high geothermal gradient in backarc lithosphere. *Tectonophysics*, *554*, 74–82.
- Yang, H., & Ghose, S. (1994). Thermal expansion, Debye temperature and Grüneisen parameter of synthetic (Fe, mg)SiO<sub>3</sub> orthopyroxenes. *Physics and Chemistry of Minerals*, *20*(8), 575–586. <https://doi.org/10.1007/BF00211853>
- Yang, H., & Ghose, S. (1995). High temperature single crystal X-ray diffraction studies of the ortho-proto phase transition in enstatite, Mg<sub>2</sub>Si<sub>2</sub>O<sub>6</sub> at 1360 K. *Physics and Chemistry of Minerals*, *22*(5), 300–310.
- Yang, H., & Prewitt, C. T. (2000). Chain and layer silicates at high temperatures and pressures. *Reviews in Mineralogy and Geochemistry*, *41*(1), 211–255. <https://doi.org/10.2138/rmg.2000.41.8>
- Ye, Y., Schwering, R. A., & Smyth, J. R. (2009). Effects of hydration on thermal expansion of forsterite, wadsleyite, and ringwoodite at ambient pressure. *American Mineralogist*, *94*(7), 899–904. <https://doi.org/10.2138/am.2009.3122>
- Zhan, Z. (2017). Gutenberg–Richter law for deep earthquakes revisited: A dual-mechanism hypothesis. *Earth and Planetary Science Letters*, *461*, 1–7. <https://doi.org/10.1016/j.epsl.2016.12.030>
- Zhang, D., Dera, P. K., Eng, P. J., Stubbs, J. E., Zhang, J. S., Prakapenka, V. B., & Rivers, M. L. (2017). High pressure single crystal diffraction at PX<sup>2</sup>. *Journal of Visualized Experiments*, *119*, e54660. <https://doi.org/10.3791/54660>
- Zhang, D., Jackson, J. M., Chen, B., Sturhahn, W., Zhao, J., Yan, J., & Caracas, R. (2013). Elasticity and lattice dynamics of enstatite at high pressure. *Journal of Geophysical Research: Solid Earth*, *118*, 4071–4082. <https://doi.org/10.1002/jgrb.50303>
- Zhang, D., Jackson, J. M., Sturhahn, W., & Xiao, Y. (2011). Local structure variations observed in orthoenstatite at high pressures. *American Mineralogist*, *96*(10), 1585–1592. <https://doi.org/10.2138/am.2011.3721>
- Zhang, J. S., & Bass, J. D. (2016). Single crystal elasticity of natural Fe-bearing orthoenstatite across a high-pressure phase transition. *Geophysical Research Letters*, *43*, 8473–8481. <https://doi.org/10.1002/2016GL069963>
- Zhang, J. S., Dera, P., & Bass, J. D. (2012). A new high-pressure phase transition in natural Fe-bearing orthoenstatite. *American Mineralogist*, *97*(7), 1070–1074. <https://doi.org/10.2138/am.2012.4072>
- Zhang, J. S., Reynard, B., Montagnac, G., Wang, R. C., & Bass, J. D. (2013). Pressure-induced *Pbca*-*P2<sub>1</sub>/c* phase transition of natural orthoenstatite: Compositional effect and its geophysical implications. *American Mineralogist*, *98*(5–6), 986–992. <https://doi.org/10.2138/am.2013.4345>
- Zhao, Y., Schiferl, D., & Shankland, T. J. (1995). A high PT single-crystal X-ray diffraction study of thermoelasticity of MgSiO<sub>3</sub> orthoenstatite. *Physics and Chemistry of Minerals*, *22*(6), 393–398.
- Zhou, W., Xie, H., Zhao, Z., & Guo, J. (2001). Garnet growth in the early stage of trachybasalt-eclogite transformation. *Chinese Physical Letters*, *18*(11), 1500.